A novel 3D GBSM for mmWave MIMO channels

Jie HUANG[1], Cheng-Xiang WANG[1,2*], Yu LIU[1], Jian SUN[1] & Wensheng ZHANG[1]

[1]*Shandong Provincial Key Lab of Wireless Communication Technologies,*
School of Information Science and Engineering, Shandong University, Qingdao 266237, China;
[2]*Institute of Sensors, Signals and Systems, School of Engineering & Physical Sciences,*
Heriot-Watt University, Edinburgh EH14 4AS, U.K.

Abstract In this paper, a novel three dimensional (3D) wideband geometry-based stochastic model (GBSM) for millimeter wave (mmWave) multiple-input multiple-output (MIMO) channels is proposed. A homogeneous Poisson point process (PPP) is used to generate the clusters in 3D space. The transmitter (Tx) and receiver (Rx) are surrounded by two spheres. The scatterers distributed in the two spheres are introduced to mimic the clustering effects of multipath components (MPCs) in delay and angular domains. The large-scale path loss model and line-of-sight (LOS) probability model are taken into account to make the channel model realistic. In addition, mmWave channel measurements are conducted in an indoor environment. Simulation results based on the two-sphere channel model are compared with measurement results and good agreements are achieved, which validates the proposed channel model. The results indicate that the proposed channel model has good adaptivity and can model the mmWave channel accurately.

Keywords 3D GBSM, mmWave channels, homogeneous PPP, LOS probability, channel measurements

1 Introduction

Millimeter wave (mmWave) communication is one of the key technologies for the fifth generation (5G) wireless communication systems [1–6]. The huge bandwidths make it possible to achieve high data transmission rate. But it also suffers from high path loss due to the increase of frequencies. Standards like IEEE 802.15.3c for wireless personal area network (WPAN) [7] and IEEE 802.11ad for wireless local area network (WLAN) [8] have been developed, and IEEE 802.11ay for next generation wireless fidelity (WiFi) [9] is being developed for 60 GHz bands around which there are at least 5 GHz unlicensed bandwidths almost all over the world. The developed channel models are mainly based on the extended Saleh-Valenzuela (S-V) model [10,11] which assumed that rays arrive in clusters in both delay and angular domains.

Recently, there are many groups trying to develop mmWave channel models for 6–100 GHz bands. Millimetre-wave evolution for backhaul and access (MiWEBA)[1]) modeled the 60 GHz channel using a quasi-deterministic (Q-D) channel model [12,13]. It is based on the fact that the channel has some Q-D components rather than is completely random. The channel impulse response (CIR) is comprised of a few Q-D strong rays (D-rays), a number of relatively weak random rays (R-rays), and flashing rays (F-rays). Mobile and wireless communications enablers for the twenty-twenty information society (METIS)

---

channel models[2)] include a map-based model, a stochastic model, and a hybrid model as a combination of both. The map-based model is a simplified ray tracing model and accounts for significant propagation mechanisms such as diffraction, specular reflection, diffuse scattering, and blockage. The stochastic model extends the geometry based stochastic model (GBSM) developed from wireless world initiative new radio (WINNER) channel model [14]. The hybrid model provides a flexible and scalable channel modeling framework. Millimetre-wave based mobile radio access network for fifth generation integrated communications (mmMAGIC) final channel model[3)] was released in May 2017. It uses an open-source software named QuaDRiGa [15] as the implementation tool and is based on extensive multi-frequency channel measurement and simulation campaigns. Some specific features such as ground reflection and blockage effects were also considered. Other channel models like 5G channel model (5GCM)[4)], 3rd generation partnership project (3GPP) TR38.901 channel model[5)], and NYU WIRELESS channel model[6)] were mainly based on some modifications or extensions of the existing WINNER II and old 3GPP channel models.

Most of the above mentioned channel models are GBSMs. The geometry-based modeling approach has been applied to channel modeling in various scenarios, such as massive multiple-input multiple-output (MIMO) [16–20], vehicle-to-vehicle (V2V) [21,22], high speed train (HST) [23–25], and unmanned aerial vehicle (UAV) [26]. GBSMs can be classified as regular-shaped [21–24] and irregular-shaped [27] ones. Regular-shaped GBSMs assume that effective scatterers are located on regular shapes, e.g., one-ring, two-ring, ellipses, and cylinders. Irregular-shaped GBSMs assume effective scatterers to be located on irregular shapes.

Though there have been extensive mmWave channel measurement campaigns [28–31], most of them are limited by the capability of the channel sounder, such as the bandwidth, frequency range, output power, system dynamic range, number of radio frequency channels, measurement time, and most important, the cost. For mmWave channels, due to the large bandwidths on the order of GHz, the delay resolution should be on the order of ns to resolve multipath components (MPCs) with near delays. MPCs are relatively sparse in space and arrive in clusters in delay and angular domains. Also, the double-directional and MIMO properties should be considered.

Different from traditional GBSMs, the proposed channel model assumes that clusters in the environment are generated by a homogeneous Poisson point process (PPP). The assumption can well model the evolution of clusters in space. In addition, the transmitter (Tx) and receiver (Rx) are assumed to be surrounded by two spheres. The scatterers are assumed to be within the sphere and confined in the volume illuminated by the related clusters to mimic the clustering effects of MPCs in delay and angular domains at both Tx and Rx sides. The delay and angle spreads can be naturally confined within limited values. Besides, the large-scale path loss model and line-of-sight (LOS) probability model are taken into account, which make the proposed channel model more practical.

The main contributions and novelties of this paper are summarized as follows:

(1) A novel three dimensional (3D) wideband GBSM is proposed for mmWave MIMO double-directional channels. Clusters are generated using a homogeneous PPP.

(2) The Tx and Rx are surrounded by two spheres to mimic the clustering effects of MPCs in both delay and angular domains. The scatterer corresponds to a ray in a cluster, with its spherical coordinates related to the delay and angle of a ray.

(3) The large-scale path loss model and LOS probability model are taken into account to make the proposed channel model realistic.

(4) Indoor mmWave channel measurements are conducted. Simulation results based on the proposed channel model are compared with measurement results and good agreements are achieved, which validates the proposed channel model.

---

2) METIS channel model. https://www.metis2020.com/wp-content/uploads/METIS_D1.4_v3.pdf.
3) mmMAGIC channel model. https://bscw.5g-mmmagic.eu/pub/bscw.cgi/d202656/mmMAGIC_D2-2.pdf.
4) 5GCM. http://www.5gworkshops.com/5GCMSIG_WhitePaper_r2dot3.pdf.
5) 3GPP channel model. http://www.3gpp.org/ftp//Specs/archive/38_series/38.901/.
6) NYU WIRELESS channel model. http://wireless.engineering.nyu.edu/nyusim/.

The remainder of this paper is organized as follows. Section 2 introduces the homogeneous PPP and describes the novel 3D mmWave GBSM. In Section 3, indoor mmWave channel measurements are introduced. Simulation results based on the proposed channel model are compared with measurement results and validations of the channel model are analyzed in Section 4. Finally, conclusions are drawn in Section 5.

2 A novel 3D wideband mmWave MIMO GBSM

2.1 Homogeneous PPP

Stochastic geometry has been widely used for system level simulations in cellular networks [32–34]. By modeling the base station (BS) and mobile station (MS) locations using spatial point processes on the two-dimensional (2D) plane, the impacts of system parameters on the key performance metrics can be analyzed. Homogeneous PPP is one of the most popular spatial point processes.

For a homogeneous PPP in a bounded region $\mathcal{A}$ of l-dimensional Euclidean space $\mathcal{R}^l$, the probability of n points existing in $\mathcal{A} \subset \mathcal{R}^l$ is given by

$$P(N(\mathcal{A}) = n) = \frac{(\Lambda |\mathcal{A}|)^n}{n!} \mathrm{e}^{-\Lambda |\mathcal{A}|}, \tag{1}$$

where $N(\mathcal{A})$ is the number of points in $\mathcal{A}$, $|\mathcal{A}|$ is the l-dimensional volume of $\mathcal{A}$, and Λ is the intensity parameter. Thus, $\Lambda |\mathcal{A}|$ denotes the expected number of Poisson points existing in $\mathcal{A}$. Homogeneous means that the intensity function Λ is a constant.

Furthermore, for a collection of disjoint and bounded Borel sets $\mathcal{A}_1, \mathcal{A}_2, \ldots, \mathcal{A}_k \subset \mathcal{R}^l$, the number of points in each set $N(\mathcal{A}_1), N(\mathcal{A}_2), \ldots, N(\mathcal{A}_k)$ are independent, i.e.,

$$P(N(\mathcal{A}_i) = n_i, i = 1, \ldots, k) = \prod_{i=1}^{k} \frac{(\Lambda |\mathcal{A}_i|)^{n_i}}{n_i!} \mathrm{e}^{-\Lambda |\mathcal{A}_i|}. \tag{2}$$

Different from traditional GBSM which assumes that clusters are distributed on the surface of regular geometry shapes, we extend the homogeneous PPP to describe the distribution of clusters in 3D space. An advantage of this method is that it can model the evolution of clusters and the non-stationary property in 3D space naturally.

2.2 A 3D mmWave MIMO GBSM

Once N clusters are generated in the 3D space with homogeneous PPP, effects of the environment are captured. Then we set the Tx and Rx antennas at predefined locations in Cartesian coordinates. To capture the clustering property of MPCs in both delay and angular domains, the Tx and Rx antennas are surrounded by two spheres. The scatterers are related with rays in each cluster which are confined by surfaces of a circular cone and a spherical segment. The circular cone and the spherical segment has the same base. The set of intersection points consists a spherical small circle, and the points are also points of tangency between the tangent line across the cluster and the sphere. The solid angle of the cone can also be calculated. Another merit of the assumption is that the delay and angle spreads of rays in each cluster are related with the radius of sphere and the distance between the cluster and the center of the sphere. Note that clusters generated by homogeneous PPP should be outside the two spheres. Moreover, the distance between any two generated clusters should be larger than a pre-defined value, which is related to the minimum delay difference between the two clusters. The proposed two-sphere channel model is illustrated in Figure 1, while definitions of channel model parameters are shown in Table 1.

As shown in Figure 1, the Tx antenna is located at the center of the sphere O_T with radius of R_T in local Cartesian coordinate system x_T–y_T–z_T with its coordinates of (x_t, y_t, z_t) given in global Cartesian coordinate system. Similarly, the Rx antenna is located at the center of the sphere O_R with radius of R_R in local Cartesian coordinate system x_R–y_R–z_R, while the coordinates of the Rx antenna are (x_r, y_r, z_r)
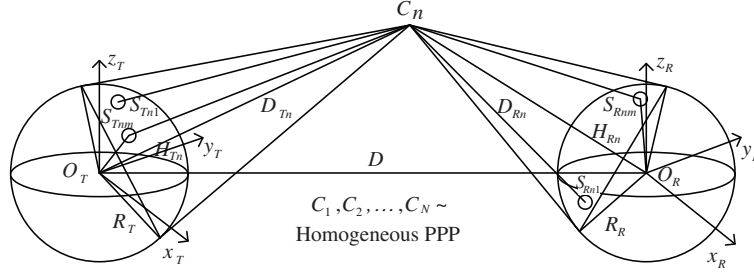
Figure 1 The proposed two-sphere mmWave channel model.

Table 1 Definitions of channel model parameters

Parameter	Definition
$O_T(x_t, y_t, z_t)$	Coordinates of the center of the Tx sphere
$O_R(x_r, y_r, z_r)$	Coordinates of the center of the Rx sphere
R_T, R_R	Radius of the Tx and Rx spheres, respectively
D	Distance between the centers of the Tx and Rx spheres
$C_n(x_n, y_n, z_n), n = 1, \ldots, N$	Coordinates of homogeneous PPP clusters
D_{Tn}	Distance between cluster C_n and the center of the Tx sphere
D_{Rn}	Distance between cluster C_n and the center of the Rx sphere
H_{Tn}, H_{Rn}	Height of the spherical segment related to C_n at Tx and Rx side, respectively
$S_{Tnm}(r_{tnm}, \phi_{tnm}, \theta_{tnm})$, $n = 1, \ldots, N, m = 1, \ldots, M_n$	Spherical coordinates of scatterers at Tx side
$S_{Rnm}(r_{rnm}, \phi_{rnm}, \theta_{rnm})$, $n = 1, \ldots, N, m = 1, \ldots, M_n$	Spherical coordinates of scatterers at Rx side

given in global Cartesian coordinate system. The distance between Tx and Rx antennas is D. The Tx antenna is used as a reference to describe the arrival and departure angles.

Suppose the n-th cluster $C_n(x_n, y_n, z_n)$ to be a light source that illuminates the Tx and Rx spheres simultaneously, the illuminated curve surface of the sphere is called the spherical crown, while H_{Tn} and H_{Rn} are the height of the spherical segments at Tx and Rx side, respectively. This is somewhat similar to the concept of receiving ball in ray tracing simulation which allows rays arrive in a ball around the receiving point.

Scatterers are assumed to be distributed in the spherical segment with height of H_{Tn}/H_{Rn} and the circular cone with its vertex of O_T/O_R. The m-th scatterer corresponding to the n-th cluster is denoted as S_{Tnm} and S_{Rnm} at Tx and Rx side, respectively. The spherical coordinates of scatterers at Tx and Rx sides are directly related with the delays and angles of rays in each cluster, which are well constricted in the limited volume of the sphere. Then, the m-th non-line-of-sight (NLOS) ray in the n-th cluster is related with the route of O_T–S_{Tnm}–C_n–S_{Rnm}–O_R. The delay and angle information of each MPC can be calculated based on the geometry relationships and the CIR can be generated.

2.3 CIR generation

2.3.1 *LOS path*

From the proposed channel model, the LOS path distance is

$$D = |O_T O_R| = \sqrt{(x_t - x_r)^2 + (y_t - y_r)^2 + (z_t - z_r)^2}, \tag{3}$$

and the LOS path delay is

$$\tau_0 = \frac{D}{c}, \tag{4}$$

where $c = 3 \times 10^8$ m/s is the speed of light.

To make the proposed channel model realistic, the large-scale close-in path loss model is considered and given as [35]

$$\text{PL}(d)[\text{dB}] = 20\log_{10}\left(\frac{4\pi d_0}{\lambda}\right) + 10\overline{n}\log_{10}\left(\frac{d}{d_0}\right) + X_\sigma \quad (d \geqslant d_0),\tag{5}$$

where d is the Tx–Rx distance, d_0 is the free space reference distance, $\lambda = c/f_c$ is the wavelength with f_c denotes the carrier frequency, $\overline{n}$ is the path loss exponent, and X_σ is the typical log-normal shadowing fading (SF) with 0 dB mean and standard deviation of σ dB.

The LOS path amplitude in linear is then given as

$$\alpha_0 = 10^{\frac{-\text{PL}(D)}{20}},\tag{6}$$

and the LOS path phase ψ_0 is assumed to be uniformly distributed, i.e., $\psi_0 \sim U[0, 2\pi]$.

For LOS path, the azimuth angle of departure (AAoD) and azimuth angle of arrival (AAoA) are the same and can be calculated as

$$\phi_0 = \begin{cases} \arccos\left(\dfrac{x_r - x_t}{\sqrt{(x_r - x_t)^2 + (y_r - y_t)^2}}\right), & y_r \geqslant y_t, \\ -\arccos\left(\dfrac{x_r - x_t}{\sqrt{(x_r - x_t)^2 + (y_r - y_t)^2}}\right), & \text{else.} \end{cases}\tag{7}$$

The LOS path elevation angle of departure (EAoD) and elevation angle of arrival (EAoA) are the same and can be calculated as

$$\theta_0 = \arcsin\left(\frac{z_r - z_t}{\sqrt{(x_r - x_t)^2 + (z_r - z_t)^2}}\right),\tag{8}$$

and we denote the departure/arrival angle of LOS path as $\Omega_0 = [\phi_0, \theta_0]$ for convenient.

Also, the LOS probability is considered as it is an integral part of channel models for cellular network design and evaluation [36]. In [36], the LOS probability of mmWave channel in open square, shopping mall, and office environments was evaluated. The proposed generic exponential LOS probability model is adopted here as

$$P_0(d) = (1 - P_\infty)\mathrm{e}^{-(d/\alpha)^\beta} + P_\infty,\tag{9}$$

where P_∞ is the probability when the distance d tends to be infinity, α is the decay parameter, and β is the exponent parameter.

2.3.2 *NLOS paths*

For NLOS components, only the route O_T–S_{Tnm}–C_n–S_{Rnm}–O_R is considered. The delays and angles are then calculated according to the geometry relationships.

The distances between cluster S_n and Tx/Rx are given as

$$D_{Tn} = |O_T C_n| = \sqrt{(x_n - x_t)^2 + (y_n - y_t)^2 + (z_n - z_t)^2},\tag{10}$$

$$D_{Rn} = |O_R C_n| = \sqrt{(x_n - x_r)^2 + (y_n - y_r)^2 + (z_n - z_r)^2}.\tag{11}$$

The heights of the spherical segment corresponding to cluster C_n at Tx and Rx sides are given as

$$H_{Tn} = R_T - R_T^2/D_{Tn},\tag{12}$$

$$H_{Rn} = R_R - R_R^2/D_{Rn}.\tag{13}$$

The surface areas of the spherical crown corresponding to cluster C_n at Tx side is $2\pi R_T H_{Tn}$, thus the solid angle at Tx side which confines the distribution of scatterers is $2\pi R_T H_{Tn}/R_T^2 = 2\pi(1 - R_T/D_{Tn})$. Similarly, the solid angle at Rx side is $2\pi(1 - R_R/D_{Rn})$.

Based on the above geometry relationships, the number of rays in each cluster, i.e., the number of scatterers is assumed to be Poisson distributed, i.e., $M_n \sim \text{Poisson}(\overline{M}_n)$, with mean value of $\overline{M}_n = \gamma(2 - R_T/D_{Tn} - R_R/D_{Rn})$, where γ is a scaling parameter to control the number of rays in each cluster. Note that the scatterers are paired at Tx and Rx sides automatically when they are generated. The spherical coordinates of the m-th scatterer corresponding to the n-th cluster, i.e., $S_{Tnm}(r_{tnm}, \phi_{tnm}, \theta_{tnm})$ and $S_{Rnm}(r_{rnm}, \phi_{rnm}, \theta_{rnm})$ are assumed to be distributed in the confined space.

The distance between the Tx center and the corresponding scatterer S_{Tnm} is assumed to be uniformly distributed in the sphere, i.e., $r_{tnm} \sim U[0, R_T]$. Similarly, the distance between the Rx center and the corresponding scatterer S_{Rnm} is also uniformly distributed in the sphere as $r_{rnm} \sim U[0, R_R]$. Thus, the delay of the m-th ray in the n-th cluster is $\tau_{nm} = (D_{Tn} + D_{Rn} + r_{tnm} + r_{rnm})/c$. Note that the delay differences in each cluster are well confined by the radii of the two spheres and they should be much less than the delay resolution of the channel.

The von Mises distribution is widely used in probability theory and directional statistics. As it is a close approximation to the wrapped normal distribution which is the circular analogue of the normal distribution, it is also known as the circular normal distribution[7]. The von Mises distribution is given as follows:

$$f(x|\mu, \kappa) = \frac{e^{\kappa \cos(x-\mu)}}{2\pi I_0(\kappa)}, \tag{14}$$

where μ is a measure of location, κ is a measure of concentration, and $I_0(\cdot)$ is the modified Bessel function of order 0. The parameters μ and $1/\kappa$ are analogous to the mean and variance in the normal distribution. The probability distribution function (PDF) of von Mises distribution is periodic in 2π, thus it is suitable to describe the angle distribution. When κ is zero, it becomes uniform distribution, and for small κ, it is close to uniform distribution. The distribution becomes very concentrated around the angle μ with κ being a measure of the concentration and approaches a normal distribution as κ increases.

Take the Tx side as an example. Firstly, the center azimuth and elevation angles corresponding to cluster C_n are given as

$$\phi_{tn} = \begin{cases} \arccos\left(\dfrac{x_n - x_t}{\sqrt{(x_n - x_t)^2 + (y_n - y_t)^2}}\right), & y_n \geqslant y_t, \\[4mm] -\arccos\left(\dfrac{x_n - x_t}{\sqrt{(x_n - x_t)^2 + (y_n - y_t)^2}}\right), & \text{else}, \end{cases} \tag{15}$$

$$\theta_{tn} = \arcsin\left(\frac{z_n - z_t}{\sqrt{(x_n - x_t)^2 + (z_n - z_t)^2}}\right). \tag{16}$$

Then, the relative azimuth and elevation angles are generated according to von Mises distributions as

$$\phi'_{tnm} \sim f\left(x\Big|0, \frac{D_{Tn}}{\eta R_T}\right), \tag{17}$$

$$\theta'_{tnm} \sim f\left(x\Big|0, \frac{D_{Tn}}{2\eta R_T}\right), \tag{18}$$

where η is a scaling parameter to control the concentration/spreading of angles. Note that the generated angles are distributed in $[-\pi, \pi]$. The generated angles are then scaled to obtain the real scatterer angles as follows:

$$\phi_{tnm} = \phi_{tn} + \phi'_{tnm} \arccos(R_T/D_{Tn})/\pi, \tag{19}$$

$$\theta_{tnm} = \theta_{tn} + \theta'_{tnm} \arccos(R_T/D_{Tn})/(2\pi). \tag{20}$$

For the generated azimuth angle, if it is larger than π, it will be replaced by $\phi_{tnm} - 2\pi$, and replaced by $\phi_{tnm} + 2\pi$ if it is smaller than $-\pi$. For the generated elevation angle, if it is larger than $\pi/2$, it will be replaced by $\pi - \theta_{tnm}$, and replaced by $-\theta_{tnm} - \pi$ if it is smaller than $-\pi/2$.

---

7) Wikipedia. https://en.wikipedia.org/wiki/Von_Mises_distribution.

Similarly, the angles at Rx side are given as

$$\phi_{rnm} = \phi_{rn} + \phi'_{rnm}\arccos(R_R/D_{Rn})/\pi, \tag{21}$$

$$\theta_{rnm} = \theta_{rn} + \theta'_{rnm}\arccos(R_R/D_{Rn})/(2\pi), \tag{22}$$

$$\phi_{rn} = \begin{cases} \arccos\left(\dfrac{x_r - x_n}{\sqrt{(x_n - x_r)^2 + (y_n - y_r)^2}}\right), & y_r \geqslant y_n, \\[4mm] -\arccos\left(\dfrac{x_r - x_n}{\sqrt{(x_n - x_r)^2 + (y_n - y_r)^2}}\right), & \text{else}, \end{cases} \tag{23}$$

$$\theta_{rn} = \arcsin\left(\frac{z_r - z_n}{\sqrt{(x_n - x_r)^2 + (z_n - z_r)^2}}\right), \tag{24}$$

$$\phi'_{rnm} \sim f\left(x\Big|0, \frac{D_{Rn}}{\eta R_R}\right), \tag{25}$$

$$\theta'_{rnm} \sim f\left(x\Big|0, \frac{D_{Rn}}{2\eta R_R}\right). \tag{26}$$

The generated azimuth and elevation arrival angles will be transformed similar to departure angles to be located in the range of $[-\pi, \pi]$ and $[-\pi/2, \pi/2]$, respectively. For the m-th ray in the n-th cluster, we denote the departure and arrival angles as $\Omega_{tnm} = [\phi_{tnm}, \theta_{tnm}]$ and $\Omega_{rnm} = [\phi_{rnm}, \theta_{rnm}]$, respectively. Similar to the definition in [37], we assume that the ray with a larger delay has a smaller power. Then, the amplitude of the m-th ray in the n-th cluster is given as

$$\alpha_{nm} = \frac{\xi e^{-\tau_{nm}/\tau_n^{\min}}}{4\pi f_c \tau_{nm}}, \tag{27}$$

where ξ is the reflection coefficient, $\tau_n^{\min}$ is the minimum delay in the n-th cluster, and $e^{-\tau_{nm}/\tau_n^{\min}}$ is used to model the exponential decay of power with delay. The phase of the m-th ray in the n-th cluster is assumed to be uniformly distributed, i.e., $\psi_{nm} \sim U[0, 2\pi]$.

2.3.3 *Complete CIR*

The CIR is given as

$$\begin{aligned} h(\tau, \Omega_t, \Omega_r) = {}& \varepsilon(P_0(D) - u)\alpha_0 e^{j\psi_0}\delta(\tau - \tau_0)\delta(\Omega_t - \Omega_0) \\ & + \sum_{n=1}^{N}\sum_{m=1}^{M_n} \alpha_{nm} e^{j\psi_{nm}}\delta(\tau - \tau_{nm})\delta(\Omega_t - \Omega_{tnm})\delta(\Omega_r - \Omega_{rnm}), \end{aligned} \tag{28}$$

where $\varepsilon(\cdot)$ is the step function

$$\varepsilon(t) = \begin{cases} 1, & t > 0, \\ 0, & \text{else}, \end{cases} \tag{29}$$

and u is a random variable uniformly distributed in [0,1].

2.4 MIMO channel generation

After the generation of the double-directional CIR for single Tx and Rx antennas, the wideband MIMO channel can be synthesized. As an example, suppose the Tx side is equipped with P-element uniform linear array with separation space of Δd_t, and the Rx side is equipped with Q-element uniform linear array with separation space of Δd_r, and K frequency points are sampled in a bandwidth of B. Thus the sampled frequency point is

$$f_k = f_c - \frac{B}{2} + \frac{B(k-1)}{K-1}, \quad k = 1, \ldots, K, \tag{30}$$

and the MIMO channel transfer function (CTF) matrix can be given as

$$H(p, q, k) = \varepsilon(P_0(D) - u)H^{\mathrm{LOS}}(p, q, k) + H^{\mathrm{NLOS}}(p, q, k), \tag{31}$$
$$p = 1, \ldots, P, \quad q = 1, \ldots, Q, \quad k = 1, \ldots, K,$$

with

$$H^{\mathrm{LOS}}(p, q, k) = \alpha_0 \exp[\mathrm{j}(\psi_0 - 2\pi f_k \tau_0)]\exp[\mathrm{j}2\pi/\lambda(\langle e(\Omega_0), \Delta d_t(p-1)\rangle + \langle e(\Omega_0), \Delta d_r(q-1)\rangle)], \tag{32}$$

$$H^{\mathrm{NLOS}}(p, q, k) = \sum_{n=1}^{N}\sum_{m=1}^{M_n}\alpha_{nm}\exp[\mathrm{j}(\psi_{nm} - 2\pi f_k \tau_{nm})]\exp[\mathrm{j}2\pi/\lambda(\langle e(\Omega_{tnm}), \Delta d_t(p-1)\rangle \tag{33}$$
$$+ \langle e(\Omega_{rnm}), \Delta d_r(q-1)\rangle)],$$

and

$$\langle e(\Omega), \Delta d\rangle = \Delta d_x \cos\phi \sin\theta + \Delta d_y \sin\phi \sin\theta + \Delta d_z \cos\theta, \tag{34}$$

where $\Omega = [\phi, \theta]$ denotes the azimuth and elevation angles, and $\Delta d = [\Delta d_x, \Delta d_y, \Delta d_z]$ denotes the coordinates of the antenna element in the antenna array.

For each CTF corresponding to the p-th Tx antenna element and q-th Rx antenna element, the CIR is obtained by the inverse fast Fourier transform (IFFT), i.e.,

$$h(p, q, 1:K) = \mathrm{IFFT}(H(p, q, 1:K)), \quad p = 1, \ldots, P, \quad q = 1, \ldots, Q. \tag{35}$$

3 Indoor mmWave channel measurements

3.1 Measurement environment

The channel measurements are conducted in an indoor office environment in Shandong University, China, with room size of 7.2 m×7.2 m×3 m, as shown in Figure 2(a) [38, 39]. The layout and sizes of objects in the office are shown in Figure 2(b). The office is furnished with chairs, desks, and computers. There are some windows on both sides of the wall.

3.2 Measurement system setup

The measurement system consists of a Keysight N5227A vector network analyzer (VNA), antennas, an antenna positioner, cables, and a laptop. The measured S_{21} parameter is the CTF between Tx and Rx, and the CIR can be obtained by the inverse Fourier transform. The antenna locations are shown in Figure 2(b). The coordinate of the Rx antenna is (1, 3, 1.45), and the coordinates of Tx antennas are Tx1(4, 2.2, 2.6), Tx2(3.2, 2.4, 2.6), Tx3(3.6, 3, 2.6), and Tx4(2, 5.2, 2.6). The 11, 16, 28, and 38 GHz bands were measured. For each frequency band, the antenna gain is 10 dBi with a half power beamwidth (HPBW) of 55°. The Rx antenna is a 3 dBi vertical polarized biconical antenna working at 3–40 GHz bands. A back-to-back calibration is conducted before the measurement at each Tx antenna location.

4 Simulation results and analysis

Based on the proposed channel model, simulations are conducted in the same indoor office environment with channel measurements. Detailed values of the simulation parameters for Tx1 at 16 GHz are shown in Table 2.

In the simulation, the clusters are distributed in the office environment with the same size. The clusters are assumed to be effective representatives of objects in the environment. The Tx and Rx antennas are located at the same positions with the measurement. The mean number of clusters is 8. The carrier frequency is set as 16 GHz. The bandwidth and frequency points are the same with the measurement. The path loss model and LOS probability model parameters are similar with measurement results in [40] and [36], respectively. A Gaussian noise with mean value of −100 dB and deviation of 3 dB has been added to compare with the channel measurements.
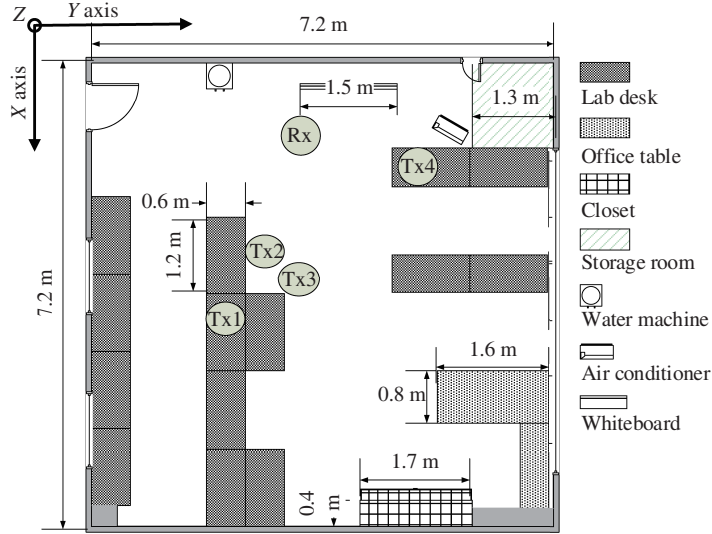
Figure 2 (Color online) (a) Photo and (b) layout of the environment.

Table 2 Values of simulation parameters

Parameter	Value
Room size, $L_x \times L_y \times L_z$ (m^3)	7.2×7.2×3
Tx sphere center, $O_T(x_t, y_t, z_t)$	(1, 3, 1.45)
Rx sphere center, $O_R(x_r, y_r, z_r)$	(4, 2.2, 2.6)
Tx sphere radius, R_T (m)	0.3
Rx sphere radius, R_R (m)	0.3
Number of Tx antenna elements, P	20
Number of Rx antenna elements, Q	20
Tx antenna element space, Δd_t (m)	0.5λ
Rx antenna element space, Δd_r (m)	0.5λ
Cluster intensity, Λ	8/(7.2×7.2×3)
Carrier frequency, f_c (GHz)	16
Bandwidth, B (GHz)	2
Frequency points, K	401
Path loss model parameters	d_0=1 m, $\bar{n}$=1.8, σ=3 dB
LOS probability model parameters	α=3, β=2, P_∞=0.2
Ray number scaling parameter, γ	6
Reflection coefficient, ξ	0.8
Angle spread scaling parameter, η	3
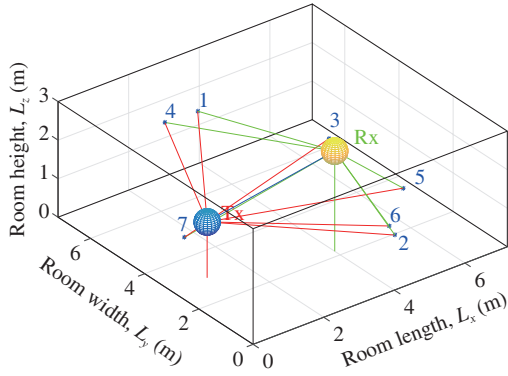
Figure 3 (Color online) Simulated room layout and clusters distribution.
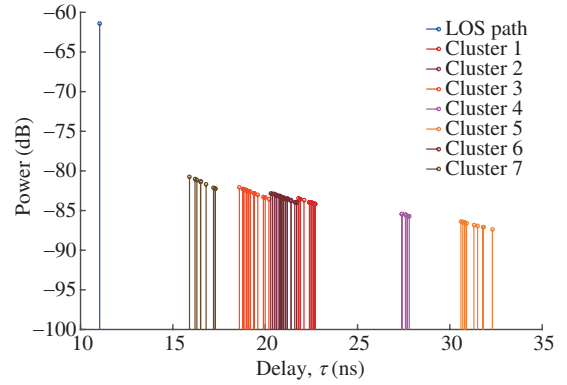
Figure 4 (Color online) Simulated discrete PDP.
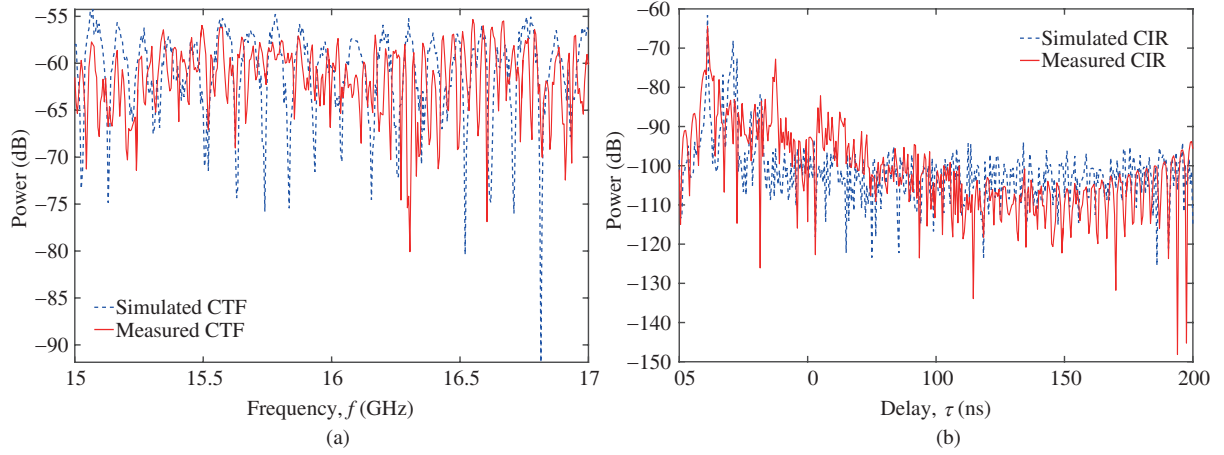
Figure 5 (Color online) Simulated and measured (a) CTFs, and (b) CIRs.

## 4.1 Comparison and validation with measurements

An example of the simulated room layout and clusters distribution is shown in Figure 3. As can be seen, seven clusters are generated. The simulated discrete power delay profile (PDP) is shown in Figure 4. Apart from the LOS path, seven clusters are generated corresponding to the seven clusters and distinguished with different colors. Different clusters have different number of rays, and rays in different clusters can have different power decay rates related with path delays. It is more realistic than the widely used S-V model which uses a single ray power decay rate for different clusters.

In Figure 5(a), the simulated CTF and the measured CTF are shown and compared. The simulated CTF is synthesized from MPC parameters as shown in (31)–(34). As seen in Figure 5(a), the simulated and measured CTFs show similar power level and frequency selectivity, which validates that the proposed channel model can well model the indoor mmWave channel.

The simulated and measured CIRs are shown in Figure 5(b). The simulated CIR is obtained from simulated CTF via IFFT. The LOS path is accurately captured, and the reflected MPCs also show similar power levels and delays.

4.2 MPCs distribution

The delay and angular domain MPC parameters can be calculated according to the proposed channel model. The simulated delay and angle of departure profile is shown in Figure 6(a), and the simulated delay and angle of arrival profile is shown in Figure 6(b). Both the color and size of circles indicate the
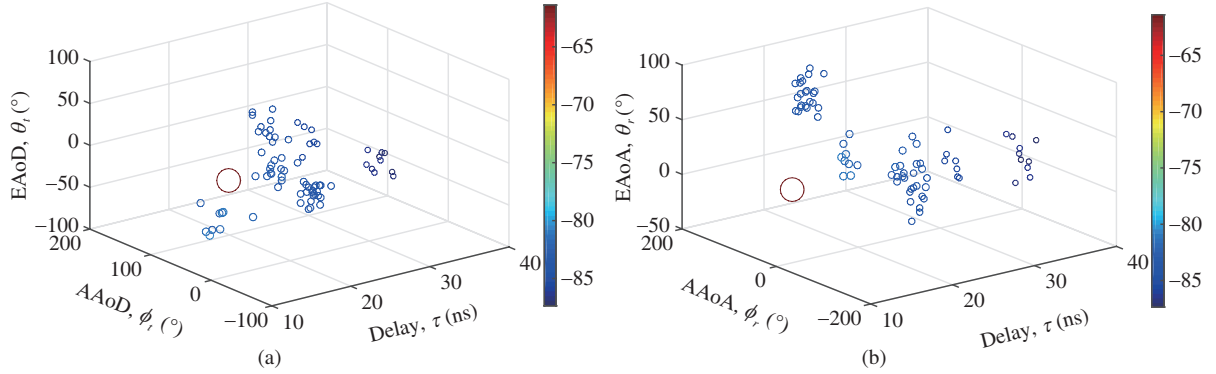
Figure 6 (Color online) Simulated delay and angle of (a) departure profile, and (b) arrival profile.
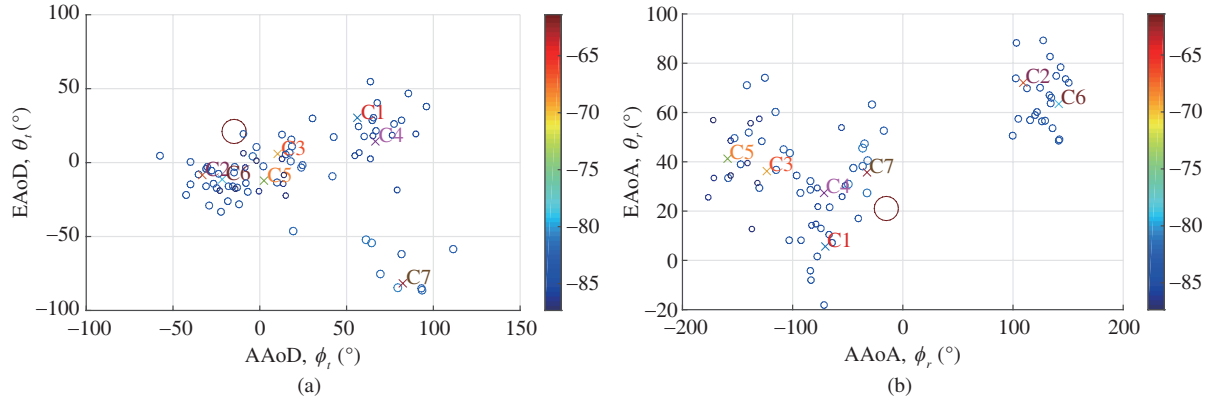
Figure 7 (Color online) Simulated joint distribution of (a) AAoD and EAoD, (b) AAoA and EAoA.

power of MPCs. The departure and arrival angles also show clustering properties in both azimuth and elevation angle domains.

The joint distribution of AAoD and EAoD is shown in Figure 7(a), and the joint distribution of AAoA and EAoA is shown in Figure 7(b). Naturally, the delay and angle information corresponding to the route O_T–C_n–O_R is assumed to be the center of the n-th cluster. Thus, the channel model can auto clustering MPCs and relate to clusters. Each cluster center is denoted by a cross in Figure 7. Table 3 summarizes the simulation results for Tx1 at 16 GHz, including the LOS/NLOS state, number of clusters, number of rays in each cluster, center of clusters, delay spread (DS), azimuth angle of departure spread (ADS), elevation angle of departure spread (EDS), azimuth angle of arrival spread (AAS), and elevation angle of arrival spread (EAS).

Some observations can be found from the simulation results: each cluster has different number of rays; each cluster spreads in delay and angular domains with different sizes; the distances between different clusters are different; clusters can overlap in delay and angular domains if two clusters are near.

4.3 Delay and angle statistical properties

The channel statistical properties including the distribution of delay and angle spreads are obtained from 500 times of Monte Carlo simulations. The simulated root mean square (RMS) DS is shown in Figure 8 and the simulated RMS angle spreads (ASs) are shown in Figure 9. It can be clearly shown that their PDFs are well fitted by Gaussian distributions. As the distance between Tx1 and Rx is about 3 m, Tx1 location has a large probability to be in LOS state, the RMS DS is relatively small and within 10 ns. The RMS ASs including RMS ADS, EDS, AAS, and EAS also have good agreement with channel measurements.

Table 3 Simulation results for Tx1 at 16 GHz

Parameter	Value
LOS/NLOS state	LOS
Number of clusters	7
Number of rays in each cluster	[12, 10, 15, 7, 10, 13, 9]
Center of clusters	C1(22.5 ns, 56.3°, 30.1°, −70.5°, 5.6°)
	C2(21.0 ns, −33.2°, −8.4°, 109.5°, 72.1°)
	C3(19.3 ns, 10.4°, 5.8°, −123.4, 36.2°)
	C4(27.7 ns, 66.6°, 14.3°, −71.7°, 27.5°)
	C5(31.3 ns, 2.5°, −12.4°, −159.0°, 41.3°)
	C6(21.1 ns, −21.5°, −11.2°, 141.8°, 63.6°)
	C7(16.8 ns, 82.5°, −81.7°, −32.2°, 35.7°)
Delay and angle spreads	DS: 3.7 ns
	ADS: 44.1°, EDS: 32.7°
	AAS: 105.7°, EAS: 22.5°
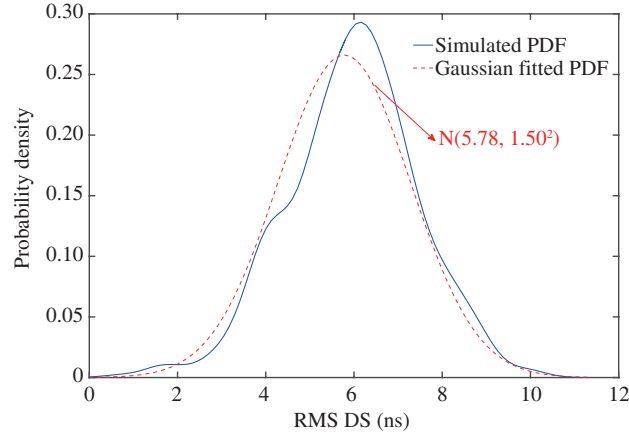
Figure 8 (Color online) Simulated and Gaussian fitted PDFs of RMS DS.

4.4 Effects of channel model parameters

The room size, Tx sphere center, Rx sphere center, and carrier frequency are related to the real measurement environment layout. The Tx and Rx sphere radii control the cluster spread in delay domain. The cluster intensity affects the number of clusters. The ray number scaling parameter influences the number of rays in each cluster. The reflection coefficient is related to the power of each MPC. The angle spread scaling parameter controls the cluster spread in azimuth and elevation angular domains. Thus, the model parameters have clear physical meanings and can be tuned to well fit the channel measurement data.

Based on the measurement results [41], the main difference between different mmWave bands lies in the power level and cluster power decay rate, while the RMS DS and AS have no great dependence and clear trend with frequency, the proposed mmWave channel model is applicable to different mmWave bands.

4.5 Extension to outdoor and time-varying scenarios

As clusters are generated in a given 3D space following the homogeneous PPP, the proposed channel model can also be applied to outdoor scenarios. The advantage of using homogeneous PPP is that the evolution of clusters in spatial domain can be observed.

The model can also be easily extended to time-varying scenarios for two reasons: if some objects in the environment are moving, the corresponding generated clusters can be given a velocity, thus, the coordinates of clusters are time-varying, and the generated geometry relationships will be changed to capture the non-stationary property; if Tx and Rx are moving, their coordinates can be the expression
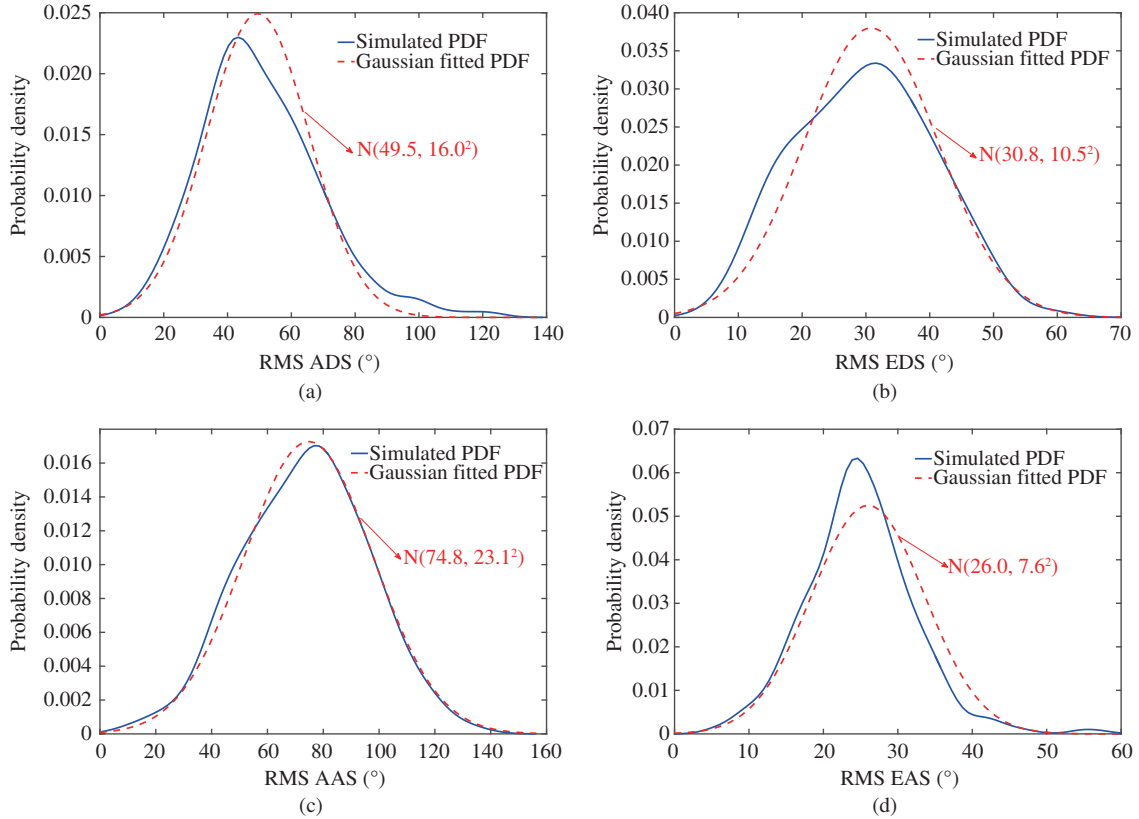
Figure 9 (Color online) Simulated and Gaussian fitted PDFs of (a) RMS ADS, (b) RMS EDS, (c) RMS AAS, and (d) RMS EAS.

of time, and the generated MPCs are changing with time. Thus, the proposed channel model can also be applied to outdoor V2V scenarios and have good adaptivity.

5 Conclusion

In this paper, we have proposed a novel 3D wideband GBSM for mmWave MIMO channels. The homogeneous PPP has been applied to the generation of clusters in 3D space to capture the evolution property of clusters. The two spheres located at Tx and Rx sides have been utilized to model the clustering effects of MPCs in both delay and angular domains. Large-scale path loss model and LOS probability model have been considered to make the channel model more practical. In addition, indoor mmWave channel measurements have been conducted. The simulation results based on the proposed channel model have been compared with measurement results, and the channel model has been verified. The results have shown that the proposed mmWave channel model is accurate and has good adaptivity.

References

1 Rappaport T S, Sun S, Mayzus R, et al. Millimeter wave mobile communications for 5G cellular: it will work! IEEE Access, 2013, 1: 335–349

2 Wang C X, Haider F, Gao X, et al. Cellular architecture and key technologies for 5G wireless communication networks. IEEE Commun Mag, 2014, 52: 122–130

3 Boccardi F, Heath R W, Lozano A, et al. Five disruptive technology directions for 5G. IEEE Commun Mag, 2014, 52: 74–80

4 Wang C X, Wu S B, Bai L, et al. Recent advances and future challenges for massive MIMO channel measurements and models. Sci China Inf Sci, 2016, 59: 021301

5 Ge X H, Tu S, Mao G Q, et al. 5G ultra-dense cellular networks. IEEE Wirel Commun, 2016, 23: 72–79

6 Feng R, Huang J, Sun J, et al. A novel 3D frequency domain SAGE algorithm with applications to parameter estimation in mmWave massive MIMO indoor channels. Sci China Inf Sci, 2017, 60: 080305

7 Yong S K. TG3c channel modeling sub-committee final report. IEEE Standard 802.15-07-0584-01-003c. 2007

8 Maltsev A. Channel models for 60 GHz WLAN systems. IEEE Standard 802.11-09/0334r8. 2010

9 Maltsev A. Channel models for IEEE 802.11ay. IEEE Standard 802.11-15/1150r9. 2016

10 Saleh A A M, Valenzuela R A. A statistical model for indoor multipath propagation. IEEE J Sel Areas Commun, 1987, 5: 128–137

11 Spencer Q H, Jeffs B D, Jensen M A, et al. Modeling the statistical time and angle of arrival characteristics of an indoor multipath channel. IEEE J Sel Areas Commun, 2000, 18: 347–360

12 Maltsev A, Pudeyev A, Karls I, et al. Quasi-deterministic approach to mmWave channel modeling in a non-stationary environment. In: Proceedings of IEEE Globecom Workshops, Austin, 2014. 966–971

13 Weiler R J, Peter M, Keusgen W, et al. Quasi-deterministic millimeter-wave channel models in MiWEBA. J Wirel Com Netw, 2016, 84: 1–16

14 Kyösti P. WINNER II Channel Models. Hoboken: John Wiley & Sons, 2008

15 Jaeckel S, Raschkowski L, Börner K, et al. QuaDRiGa: a 3-D multi-cell channel model with time evolution for enabling virtual field trials. IEEE Trans Antenn Propag, 2014, 62: 3242–3256

16 Wu S B, Wang C X, Aggoune H M, et al. A non-stationary 3-D wideband twin-cluster model for 5G massive MIMO channels. IEEE J Sel Areas Commun, 2014, 32: 1207–1218

17 Wu S B, Wang C X, Haas H, et al. A non-stationary wideband channel model for massive MIMO communication systems. IEEE Trans Wirel Commun, 2015, 14: 1434–1446

18 Wu S B, Wang C X, Aggoune H M, et al. A general 3D non-stationary 5G wireless channel model. IEEE Trans Commun, 2018. doi: 10.1109/TCOMM.2017.2779128

19 Wang C X, Bian J, Sun J, et al. A survey of 5G channel measurements and models. IEEE Commun Surv Tut, 2018. in press

20 Bian J, Sun J, Wang C X, et al. A WINNER+ based 3-D non-stationary wideband MIMO channel model. IEEE Trans Wirel Commun, 2018, 17: 1755–1767

21 Yuan Y, Wang C X, Cheng X, et al. Novel 3D geometry-based stochastic models for non-isotropic MIMO vehicle-to-vehicle channels. IEEE Trans Wirel Commun, 2014, 13: 298–309

22 Yuan Y, Wang C X, He Y J, et al. 3D wideband non-stationary geometry-based stochastic models for non-isotropic MIMO vehicle-to-vehicle channels. IEEE Trans Wirel Commun, 2015, 14: 6883–6895

23 Ghazal A, Wang C X, Ai B, et al. A nonstationary wideband MIMO channel model for high-mobility intelligent transportation systems. IEEE Trans Intel Transport Syst, 2014, 16: 885–897

24 Ghazal A, Yuan Y, Wang C X, et al. A non-stationary IMT-advanced MIMO channel model for high-mobility wireless communication systems. IEEE Trans Wirel Commun, 2017, 16: 2057–2068

25 Liu Y, Wang C X, Lopez C F, et al. 3D non-stationary wideband circular tunnel channel models for high-speed train wireless communication systems. Sci China Inf Sci, 2017, 60: 082304

26 Zeng L Z, Cheng X, Wang C X, et al. A 3D geometry-based stochastic channel model for UAV-MIMO channels. In: Proceedings of IEEE Wireless Communications and Networking Conference, San Francisco, 2017

27 Jiang H, Zhang Z C, Wu L, et al. Novel 3D irregular-shaped geometry-based channel modeling for semi-ellipsoid vehicle-to-vehicle scattering environments. IEEE Wirel Commun Lett, 2018. doi: 10.1109/LWC.2018.2829892

28 Gustafson C, Haneda K, Wyne S, et al. On mm-wave multipath clustering and channel modeling. IEEE Trans Antenn Propag, 2014, 62: 1445–1455

29 Haneda K, Järveläinen J, Karttunen A, et al. A statistical spatio-temporal radio channel model for large indoor environments at 60 and 70 GHz. IEEE Trans Antenn Propag, 2015, 63: 2694–2704

30 Rappaport T S, MacCartney G R, Samimi M K, et al. Wideband millimeter-wave propagation measurements and channel models for future wireless communication system design. IEEE Trans Commun, 2015, 63: 3029–3056

31 Ko J, Cho Y J, Hur S, et al. Millimeter-wave channel measurements and analysis for statistical spatial channel model in in-building and urban environments at 28 GHz. IEEE Trans Wirel Commun, 2017, 16: 5853–5868

32 Bai T Y, Heath R W. Analyzing uplink SINR and rate in massive MIMO systems using stochastic geometry. IEEE Trans Commun, 2016, 64: 4592–4606

33 Andrews J G, Bai T Y, Kulkarni M N, et al. Modeling and analyzing millimeter wave cellular systems. IEEE Trans Commun, 2016, 65: 403–430

34 Alkhateeb A, Nam Y H, Rahman M S, et al. Initial beam association in millimeter wave cellular systems: analysis and design insights. IEEE Trans Wirel Commun, 2017, 16: 2807–2821

35 MacCartney G R, Samimi M K, Rappaport T S. Omnidirectional path loss models in New York City at 28 GHz and 73 GHz. In: Proceedings of IEEE Annual International Symposium on Personal, Indoor, and Mobile Radio Communication, Washington, 2014. 227–231

36 Järveläinen J, Nguyen S L H, Haneda K, et al. Evaluation of millimeter-wave line-of-sight probability with point cloud data. IEEE Wirel Commun Lett, 2016, 5: 228–231

37 Pedersen T, Steinböck G, Fleury B H. Modeling of reverberant radio channels using propagation graphs. IEEE Trans Antenn Propag, 2012, 60: 5978–5988

38 Wu X Y, Wang C X, Sun J, et al. 60-GHz millimeter-wave channel measurements and modeling for indoor office environments. IEEE Trans Antenn Propag, 2017, 65: 1912–1924

39 Huang J, Wang C X, Feng R, et al. Multi-frequency mmWave massive MIMO channel measurements and characterization for 5G wireless communication systems. IEEE J Sel Areas Commun, 2017, 35: 1591–1605

40 Zhang B, Zhong Z, Zhou X, et al. Path loss characteristics of indoor radio channels at 15 GHz. In: Proceedings of European Conference on Antennas and Propagation, Davos, 2016. 1–5

41 Huang J, Feng R, Sun J, et al. Comparison of propagation channel characteristics for multiple millimeter wave bands. In: Proceedings of IEEE Vehicular Technology Conference, Sydney, 2017. 1–5